Facile synthesis and selected characteristics of two-dimensional material composed of iron sulfide and magnesium-based hydroxide layers (tochilinite)

Yuri L. Mikhlin,[a]* Roman V. Borisov,[a,c] Oleg A. Bayukov,[b] Yuriy V. Knyazev,[b] Sergey M. Zharkov,[b,c] Sergey A. Vorobyev,[a] Yevgeny V. Tomashevich,[a] Maxim N. Likhatski,[a] Anastasiya D. Ivaneeva,[a] Anton A. Karacharov,[a] Denis V. Karpov,[a] Dmitriy A. Velikanov,[b] Mikhail V. Rautskii,[b] Dmitry A. Smolyakov,[b] Anton S. Tarasov[b,c]

[a] *Institute of Chemistry and Chemical Technology, Krasnoyarsk Science Center of the Siberian Branch of the Russian Academy of Sciences, Akademgorodok, 50/24, Krasnoyarsk, 660036, Russia*

[b] *Kirensky Institute of Physics, Krasnoyarsk Science Center of the Siberian Branch of the Russian Academy of Sciences, Akademgorodok 50/38, Krasnoyarsk, 660036, Russia*

[c] *Siberian Federal University, Svobodny av. 79, Krasnoyarsk, 660041, Russia*

* corresponding author, e-mail: yumikh@icct.ru

Abstract

We report here a simple hydrothermal synthesis of 100-200 nm flakes of tochilinite $m(\mathrm{Fe}_{1-x}\mathrm{S})\cdot n(\mathrm{Mg,Fe})(\mathrm{OH})_2$ constructed by interchanging atomic sheets of iron sulfide and magnesium hydroxide as a representative of a new platform of multifunctional two-dimensional materials. The formation and characteristics of the material was studied using X-ray and electron diffraction, TEM, EDS, X-ray photoelectron and ^{57}Fe Mössbauer and UV-vis-NIR spectroscopies, measurements of magnetization, dielectric permittivity, and zeta potential of aqueous dispersions. The reliable formation of tochilinite was ensured by a large excess of sodium sulfide, which induced negative zeta potential (about -30 mV) of tochilinite dispersions, whereas the potential approached zero for nearly-stoichiometric S/Fe precursor ratios. The assembly of the metal sulfide and hydroxide sheets driven by their opposite electric charges starts immediately after mixing the reagents at room temperature. The hydroxide layers contain Fe^{3+}, not Fe^{2+}, cations, the quantity of which was reduced and increased in the range 10 to 40% of Mg^{2+} by addition of Al and Li, respectively. The Fe-deficient sulfide sheets contain comparable amounts of high-spin Fe^{3+} and Fe^{2+} centers, and minor S-S bonding. The room-temperature Mössbauer spectra were fitted with several doublets with the chemical shift of 0.35-0.4 mm/s and varying quadrupole splitting. Magnetic ordering at 4.2 K manifested by three six-line patterns with the hyperfine fields of ~290, 350 and 480 kOe attributed to overlapped Fe^{2+}-S and Fe^{3+}-OH signals, Fe^{3+}-S centers and some Fe^{3+}-O centers, respectively; a paramagnetic behavior was observed in SQUID experiments. The temperature and frequency dependences of permittivity revealed the activation energy of ~0.3 eV, probably, due to electron transitions involving Fe 3d states. A series of UV-vis absorption maxima were explained in terms of the high-index all-dielectric Mie resonance and the ligand-to-metal charge transfer alike Fe-S clusters in proteins. Prospective properties and applications of the materials are discussed.

Keywords: two-dimensional materials and phenomena, tochilinite, layered composites, photoelectron spectroscopy, Mössbauer spectroscopy

1. Introduction

Transition metal chalcogenides [1-6], layered double hydroxides (LDH) of Mg, Al, Fe and other metals [7-10], metal carbides and nitrides (MXenes) [11-14] are the most known families of two-dimensional (2D) materials, aside from graphene, in which the quasi-atomic sheets are bonded by Van-der-Waals forces [15-18]. Such materials possess unique properties of interest in various fields, e.g. electro- and photocatalysis, adsorbents, electrochemical storage of energy, electronics and so on, are extensively explored at present. The materials formed by alternating 2D sheets of incommensurate metal chalcogenides and Mg, Na, Li hydroxides, which are believed to be stacked by the opposite electrical charges, are much less studied. There exists a number of naturally occurring minerals [19-42]. Valleriite $(CuFeS_2)\cdot(Mg,Al,Fe)(OH)_2$ [19-27] and tochilinite $m\mathrm{FeS}\cdot n\mathrm{(Mg,Fe)(OH)_2}$ [30-36] are the most known and important of them; particularly, valleriite ores of Noril'sk ore provenance (Russia) are of commercial importance but not involved in the exploitation because of the lack of processing technologies. Synthetic valleriite and tochilinite have been prepared and characterized too [37-50]; however, the yields of the target substances were lower than 50%, and those were substantially contaminated by the reaction by-products. Another group of layered iron chalcogenide-hydroxide materials with the composition $Fe(Se,S)\cdot(Li,Fe)OH$ and some their derivatives [51-55] synthesized in the recent years are attracting much attention because of the superconducting properties but little efforts have been made to study other characteristics and applications.

The complicated crystalline structure of tochilinite, which is less abundant, though found in a number of terrestrial locations and also in meteorites [34-36], has been refined by Organova et al. [30,32,33,38] and other researchers [37,43]. It has been established that the iron sulfide layers are tetragonal with Fe atoms in a plane being in tetrahedral coordination with sulfide anions occurring below and above the plane (Fig. 1A), and brucite-type layers are hexagonal. The tetrahedral and hexagonal layers have been considered to be deformed, i.e. compressed and stretched, respectively [32,33], so the lattice symmetry of tochilinites is usually reduced to monoclinic or triclinic, for example, with typical parameters a = 5.35, b = 15.65, c = 10.8 Å, α = 90°, β = 95°, γ = 90°, space group Cl [33], and the chemical composition $6FeS\cdot5Mg(OH)_2$. Moreover, a deficit of Fe usually exists in the sulfide layers, and Fe and Al partially replace Mg in the hydroxide part. The electronic structure, physical characteristics and chemical behavior of the mineral remain very poor understood. Natural tochilinites are commonly believed contain Fe^{2+} cations in sulfide sheets, often in the low-spin state akin to unoxidized mackinawite FeS [56-60], and high-spin Fe^{2+} in hydroxide ones. The hydroxide layers are thought to be positively charged due to the partial substitution of divalent Mg with trivalent Al, and the iron sulfide is charged negatively [32,33,37]. Several wet chemical (principally hydrothermal) and thermal synthetic routes to tochilinite have been suggested [37-41,44-46], with the reactions performed usually under reductive atmosphere, attempting to avoid oxidation of sulfide layers and produce low-spin Fe^{2+}. However, only mixtures of the material with iron (hydr)oxides and sulfides, brucite and other impurities were obtained so far, so synthesis, examination and tailoring the properties of tochilinite remain challenging.

The metal chalcogenide-hydroxide composites emerge as a new family of multifunctional 2D materials, which can be conditionally described as an LDH matrix intercalated with regular metal chalcogenide layers or vice versa, exhibiting essentially new features. Further progress with the composites requires, first of all, a facile synthesis of pure materials. Recently [50], we proposed a hydrothermal synthesis of valleriite $(CuFeS_2)\cdot(Mg,Al,Fe)(OH)_2$, examined the effect of dopants entered magnesium hydroxide (Al, Li) or both sulfide and hydroxide layers (Co, Ni, Cr), and studied the electronic structure, physical and chemical characteristics as a function of the composition. The aims of the current research were to develop a reliable preparation procedure and to elucidate specific features of the tochilinite-type materials. We started from the protocol elaborated for valleriite [50], and modified it by varying the concentrations of precursors and dopants in order to reject the reaction by-products and to control the composition, electronic, magnetic and optical characteristics of tochilinite. In order to simplify the protocol, at this stage of research we didn't strictly deoxygenate the reaction media and sample handling environment so paramagnetic materials with high-spin Fe^{3+} and Fe^{2+} in the sulfide layers were obtained, which, nonetheless, exhibit a number of non-trivial promising properties.

2. Materials and methods

2.1. Materials and synthetic procedures

Commercial reagents of analytical grade (iron sulfate $FeSO_4\cdot7H_2O$, sodium sulfide $Na_2S\cdot9H_2O$, magnesium sulfate $MgSO_4\cdot7H_2O$, aluminum sulfate $Al_2(SO_4)_3\cdot18H_2O$, lithium hydroxide $LiOH\cdot H_2O$, cobalt chloride $CoCl_2\cdot6H_2O$, aqueous ammonia and others) were used without additional purification. Deionized water (Millipore Milli-Q grade) was utilized to prepare the reagent solutions and colloidal dispersions, and to wash the precipitates. Iron sulfate was dissolved in a small volume of water, and pre-determined quantities of freshly prepared 20% solution of Na_2S were added under agitation, precipitating metal sulfides. Magnesium hydroxide or its mixture with aluminum hydroxide or/and lithium hydroxide were precipitated by adding 25% aqueous ammonia to the metal sulfate solutions. Then the dispersions were transferred to an in-home made stainless steel autoclave with Teflon liner [50]. Alternatively, all the reagents were simultaneously loaded into the autoclave, and pH was adjusted with aqueous ammonia to ~11. Both procedures were found to lead to essentially the same results. The synthesis was performed using the atomic ratios of Fe and S precursors from 1 to 1:15, i.e., ranged from a nearly stoichiometric amount to a large excess of sulfur relative to FeS composition. The vessel (32 cm^3) was purged with Ar and sealed, rotated (8 rpm) at room temperature for about 1 h and then heated to 160 ^oC using air thermostat. After the reaction for 2 h to 100 h (typically 40 h), the autoclave was cooled in ambient atmosphere, and solid products were separated using centrifugation at 4000 Hz for 15 min (CR4000, Centurion Scientific, UK) and washed by 3-5 times by decantation in water and centrifugation. The residue was stored as a wet paste or dried in air at room temperature for examination. For preparation of tochilinite colloids, the residue (approximately 0.01 g) was dispersed in water (50 mL) under ultrasonic irradiation (22 kHz, 15 W/cm^2, 1-2 min) with a Volna-M source (Center of Ultrasound Technologies, Russia).

2.2. Characterization

X-ray powder diffraction patterns were obtained from air-dried powders with a PANalytical X'Pert Pro diffractometer using Cu Kα radiation.

Transmission electron microscopy (TEM) images, energy dispersive X-ray analysis (EDS) and selected area electron diffraction (SAED) patterns were collected with a JEM 2100 microscope (JEOL, Japan) operated at accelerating voltage of 200 kV. Particles were dispersed in ethanol, and a droplet was placed on a carbon coated Ni grid (Ted Pella Inc., USA) and dried in ambient air.

X-ray photoelectron spectra were acquired with a SPECS instrument (Germany) equipped with a PHOIBOS 150 MCD-9 analyzer operated at the pass energy of 20 eV for survey spectra and 10 eV for high-resolution spectra. Monochromatic Al Kα irradiation (1486.7 eV) of the X-ray tube was used for excitation. The spectra were acquired from the samples placed on sticky carbon tape as a wet residue after centrifugation or as a dry powder. The atomic concentrations were obtained from the survey spectra; the high-resolution spectra were fitted with Gaussian-Lorentzian peak profiles after subtraction of the Shirley-type background. Spin-orbit splitting and an intensity ratio for S $2p_{3/2,1/2}$ doublet were assumed of 1.19 eV and 2:1, respectively. The Fe 2p spectra were fitted with two sets of multiplet lines (four narrow peaks and a wider satellite) [61] for Fe^{3+} cations bonded to hydroxide and to sulfide anions; additional 2-3 peaks typically needed for better fitting are probably due to Fe^{2+}-S species, as discussed below. The energy splitting and relative intensities of the lines within the sets were put at the values almost the same as those in ref. [61]. CasaXPS software package was employed for processing the spectra. Reflection electron energy loss spectra (REELS) were collected employing a STAIB electron gun incorporated in the SPECS instrument; the width at half maximum (FWHM) of elastically reflected beam was of 0.7 eV.

^{57}Fe Mössbauer spectra were measured in a transmission mode using an MC-1104Em spectrometer (Research Institute of Physics, Southern Federal University, Russia) operated in the constant acceleration mode with triangular velocity profile. A moving ^{57}Co(Rh) source was kept at room temperature, while the absorber (dry tochilinite powder about 3 mg/cm^2 of Fe thick) was either at 20 °C or cooled down to liquid helium temperature (4.2 K) employing a CFSG-311-MESS cryostat (Kriotreid Engineering, Russia). Chemical, or isomeric, shifts (δ) are given relative to α-Fe at room temperature. The spectra composed of 512 points were processed using the UnivemMS software package. Probabilities P of quadrupole splitting Δ ($\Delta = 2\varepsilon$, ε is quadrupole shift) and magnetic hyperfine fields H were first determined from the experimental spectra and were used to generate a model spectrum and then to fit the results by varying the complete set of ultrafine parameters using the least-squares method in the linear approximation [62].

Magnetic characteristics of the samples was determined using a superconducting quantum interference device (SQUID) magnetometer [62], typically with a magnetic field of 50 Oe in field cooled (FC) and zero field cooled (ZFC) regimes in the temperature range from 4.2 K to 290 K.

The *ac* impedance measurements were carried out using an Agilent E4980A LCR meter at the frequency varied from 20 Hz to 2 MHz and the temperature ranged from 4.2 K to 300 K. Dry tochilinite samples were pressed into tablets and two electrical contacts were formed with silver-epoxy adhesive Epotek. Essentially the same results were obtained with tochilinite powder loaded into a capacitor with plain copper electrodes, so possible effect of the contacts can be dismissed.

Dynamic light scattering (DLS) and zeta potential measurements of the tochilinite hydrosols were conducted using Zetasizer Nano ZS spectrometer (Malvern Instruments, UK) at scattering angle 173° in a polycarbonate cell with Pd electrodes at 25 ^{o}C using 1 mM KCl as a background electrolyte. UV-vis-NIR absorption spectra of the hydrosols were collected in the spectral region 200 - 1400 nm in a quartz cell (1 cm) with a Shimadzu UV 3600 instrument.

3. Results

3.1. Synthesis, structure, morphology and composition of tochilinites

Fig. 1 shows an ideal atomic structure of tochilinite (A) and X-ray diffraction patterns (B) from the reaction products of the hydrothermal synthesis, including Al- and Li-doped ones. XRD demonstrates that tochilinite is the predominant crystalline material with the two major reflections at *d*-spacing of ~11 Å and 5.4 Å characteristic of (001) and (002) of tochilinite along with a number of low-intensity features at smaller *d* (higher 2Θ angles) [32-38]. Crystallographic parameters of the tochilinites (Table 1) generally agree with those reported in the literature [32,33] for a variety of natural minerals and are closer to triclinic space group C1 [33], although with somewhat increased *c* and β values (typical ones are 11.1 Å vs 10. 9 Å and ~103° vs 95°, respectively). The lattice parameters slightly vary with the proportions of reagents and dopants. The diffraction patterns also show small quantities of magnesium hydroxide (brucite) as a by-product.

TEM images (Fig. 1, C-E), selected area electron diffraction (Fig. 1, H, see also Fig. S1) and EDS data (Table 1) show that tochilinite forms flake-like particles with the lateral size of 100-200 nm and the thickness of 10-30 nm, i.e., 10-25 stacked atomic FeS-$Mg(OH)_2$ layers. Cylindrical particles reported for natural and synthetic samples [43,44] are very rare; the rod-like particles visible in some images are in fact nanoflakes rotated and exposed their edges. The interplanar distances seen at the edges are about 11 Å, in agreement with the SAED and XRD patterns. The small irregular nanoparticles located around the flakes in some samples were found using EDS and SAED to be brucite.

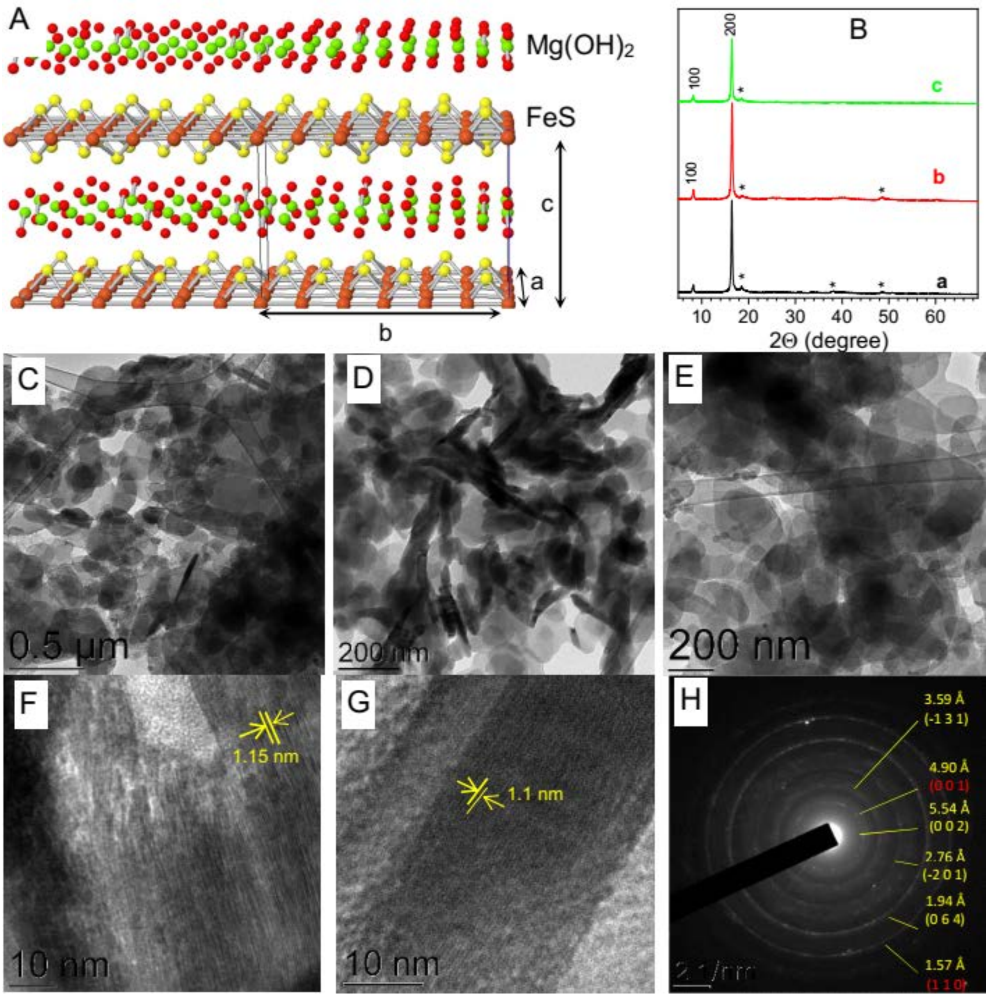

Fig. 1. A: The idealized structure of tochilinite; B: X-ray diffraction patterns of tochilinites prepared using atomic proportions of reagents (a) Fe 2, Mg 1.5, S 15, (b) Fe 2, Mg 1.5, S 15, Al 0.5, (c) Fe 2, Mg 1.5, S 15, Li 0.5 (filled circles designate reflections of brucite); TEM images acquired from C, F – sample (a), D,G – sample (b), E – sample (c); H – SAED pattern from the sample (b), reflections of brucite impurity are marked in red.

The quantity of the brucite admixture can be reduced via decreasing the relative amount of Mg precursor or partial replacing Mg with Al or Li, or reducing the initial concentration of sodium sulfide. This entails changes of the lattice parameters, i.e., decreasing the *a* and the cell volume and increasing the *b* and angle β (Table 1), that is, in effect, slightly shrinking the FeS sheets.

Table 1. Crystallographic parameters derived from XRD and average compositions (at.%) determined by EDS of tochilinite synthesized* with no dopants (a) and with addition of Al (b) or Li (c).

Sample	*a*±0.02 (Å)	*b*±0.02 (Å)	*c*±0.02 (Å)	β±0.2 (°)	*V* ($Å^3$)	Fe	S	Mg	O	Al
(a)	5.38	15.67	11.05	102.2	911	18.8	17.4	19.8	44.0	-
(b)	5.27	15.5	11.09	103.3	881	16.2	18.7	16.3	44.7	4.1
(c)	5.26	15.64	11.08	102.9	890	26.6	24.1	19.6	29.7	-

*Initial atomic proportions of Fe-, Mg-, S-, Al-, and Li- bearing reagents: (a) Fe 2, Mg 1.5, S 15, (b) Fe 2, Mg 1.5, S 15, Al 0.5, (c) Fe 2, Mg 1.5, S 15, Li 0.5.

The average chemical compositions of representative samples as determined using EDS analysis are also presented in Table 1. The compositions are in general agreement with those reported in the literature previously [30-33], somewhat varying due to different content of Fe in the hydroxide layers of tochilinite; the data also imply negligible total amounts of $Mg(OH)_2$ admixture. The relative concentrations of S indicate that iron sulfide layers are depleted in Fe, taking in mind that up to 40% of iron is located in hydroxide layers (see XPS data below). The concentration of oxygen seems decreased relative to $Mg(OH)_2$ because brucite-type structures easily lost water during ageing; errors in EDS analysis of light elements may play the role too. The low content of O in lithium-doped material likely results from incorporation of monovalent Li^+ cations into the magnesium hydroxide sheets (Li content cannot be analyzed with EDS). The effect of dopants on the tochilinite composition and properties will be further discussed below. The elements, including Al dopant, are uniformly distributed in the particles as evidenced by the EDS elemental maps presented in Fig. S2 (Supporting Information). Such dopants as Co and Ni, albeit entered both sulfide and hydroxide layers, also form their own phases at the ratios Co(Ni) to Fe larger than 0.25, and are not considered in this paper.

3.2. X-ray photoelectron spectroscopy

The XPS spectra (Fig. 2) shed light onto the chemical state of elements in tochilinites synthesized under varying conditions; the surface concentrations determined from the survey spectra are given in Table S1. In contrast to EDS, the concentrations of magnesium and sulfur are about twice as high as those of iron, probably owing to the surface sensitivity of XPS having the probing depth of 2-5 nm. XPS also found minor quantities of sodium. The effects can be attributed to small $Mg(OH)_2$ nanoparticles adhered to tochilinite flakes, and Na cations and sulfide anions adsorbed on the surface or/and trapped in the solution remnants. Noteworthyhy, the excessive concentrations of these elements decrease for the samples prepared with reducing the precursor proportion Fe/S toward 1.

The S $2p_{3/2,1/2}$ bands consist of the major doublets (from 60% to more than 80% of the total intensity) with the binding energy of S $2p_{3/2}$ peak of 161.65±0.1 eV, which is due to monosulfide anions, is well reproduced for different samples. The spectra are better fitted with additional doublets at 162.6 eV and near 163.5 eV, which arise from minor S-S bonding. The first, “disulfide” component is believed [50, 64-68] to originate from terminal atoms bearing higher negative charge in $^{-}S\text{-}S_n\text{-}S^{-}$ anions rather than central “polysulfide” atoms, and their relative intensities suggest that trisulfide anions form in the iron-deficient sulfidic layers. A wide maximum between 164 eV and 165 eV seems to be a satellite related to electron transfer onto empty Fe 3d states [50, 64-68]. The components of oxysulfur species at the BE above 168 eV are usually weak and arise from adsorbed sulfate.

The signals of OH^- groups at 531.7 eV dominate the O 1s spectra, which also comprise of the features from adsorbed water and carbonaceous contaminations (533.5 eV) and a small, less than 3-5 rel.%, component of O^{2-} in hydroxide layers, which, however, notably increases if ferric (hydr)oxides formed due to violations of the process or post-synthetic oxidation. It also is worth noting that C 1s line from adventitious aliphatic contaminations is shifted to higher binding energies by 0.2-0.5 eV even if a slow electron flood gun has been utilized. This may be indicative of a potential difference between the surface hydroxide layers and underlying FeS layers.

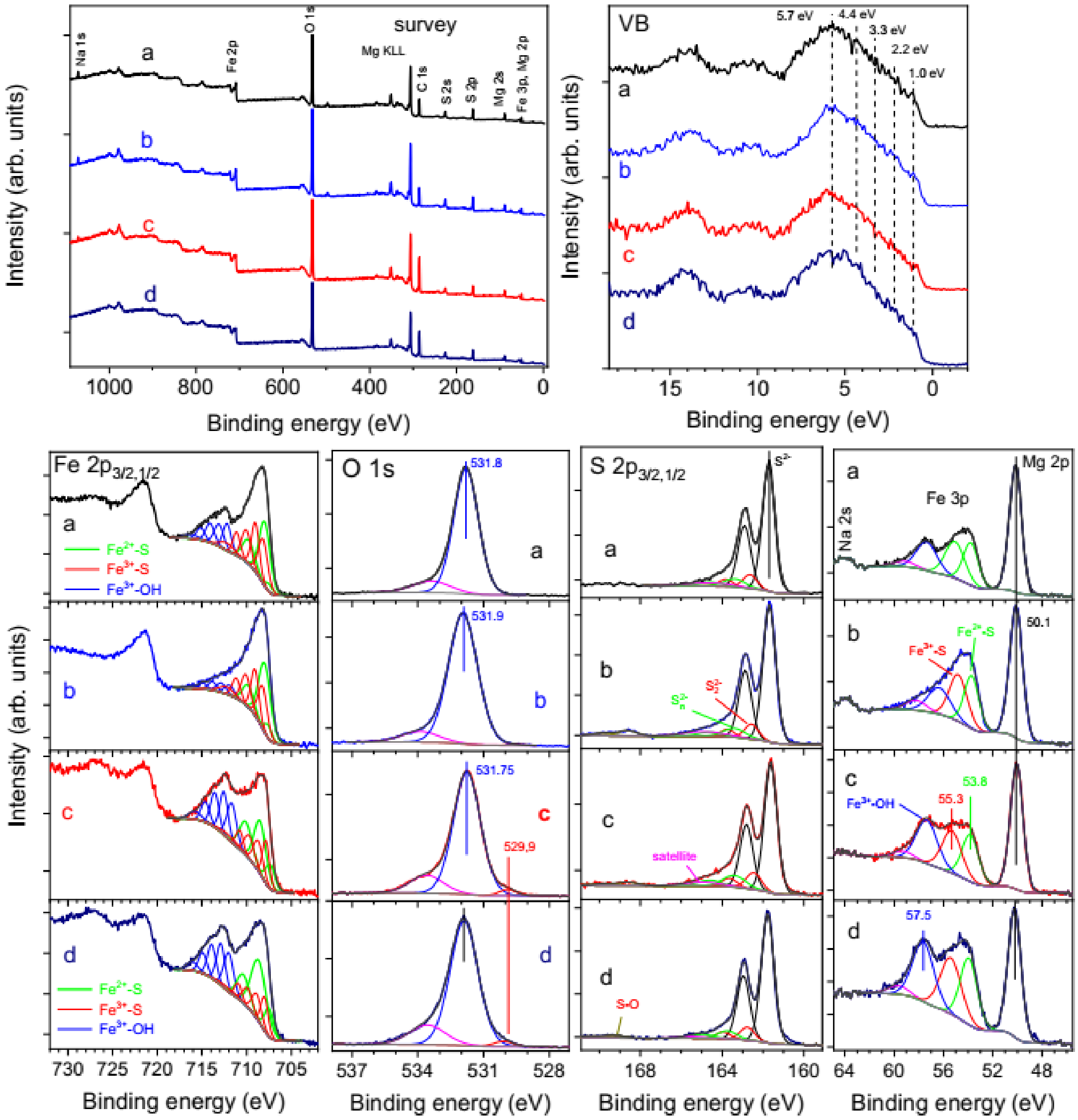

Fig. 2. X-ray photoelectron spectra of tochilinites synthesized with the atomic proportions of precursors (a) Fe 2, Mg 1.5, S 15, (b) Fe 2, Mg 1.5 Al 0.5, S 15, (c) Fe 2, Mg 1.5, Li 0.5, S 15, (d) Fe 2, Mg 1.7, S 3.

Interpretation of the Fe 2p spectra is complicated because of the presence of several chemical forms of iron and their multiplet structure [61,64]. The high-energy spectral region (710-716 eV) is well fitted with a set of four narrow lines and a wider satellite from high-spin Fe^{3+} [61] in octahedral sites of the hydroxide layers. The share of the OH-bonded Fe decreases from 20-25% down to 10-15% of total iron for undoped tochilinite for Al-modified one and that increases to more than 40 rel. % for tochilinite prepared with addition of Li. The same trend was observed for valleriite [50]; it can be explained in terms of modification of the magnesium hydroxide structure via insertion of larger (Al^{3+}) or smaller cations (Li^{+}), although exact mechanisms are still unclear. Deconvolution of the low-energy part of the Fe $2p_{3/2}$ band is ambiguous. The band can be fitted using a similar 4-line pattern from Fe^{3+} bonded to sulfur with the first peak at about 708 eV, similar to iron in chalcopyrite $CuFeS_2$ and valleriite [50,67,68], along with additional maxima at 708 eV and weaker ones at ~707.5 eV and 709.8 eV. The features can be assigned to a multiplet set of lines of high-spin Fe^{2+}-S species [61,64], however, other species like low-spin Fe^{2+} or Fe^{2+}-O, respectively, may contribute too. Moreover, the fits are not unique both in terms of relative intensities of these maxima and alternative patterns. In particular, the low-energy spectral regions can be satisfactorily fitted (Fig. S3) using three maxima at 707.5 eV and 709 eV of comparable intensities and smaller peak at 710.5 eV, which may be tentatively attributed to Fe^{2+}-S, Fe^{3+}-S and Fe^{2+}-O centers, respectively.

We also measured the spectral region of the Fe 3p and Mg 2p bands. The Fe 3p band can be described using three comparable maxima at 53.8 eV, 55 eV and 57 eV along with a minor high-energy tail. The relative intensity of the peak at about 57 eV correlates with those of Fe^{3+}-OH species in the Fe 2p spectra, depending on the presence of Al, Li, Co dopants and other conditions. The two maxima at lower energies can be associated with Fe^{2+}-S and Fe^{3+}-S centers in the sulfide layers. Again, the fitting results and assignments are not unequivocal and minor components may be missed because of broadness of Fe 3p lines, as well as the lack of reliable reference data in the literature. Nevertheless, the relative content of the species attributable to Fe^{2+} and Fe^{3+} in the sulfide layers is roughly equal in all the spectra.

The position of the Mg 2p peak at 50.1 eV insignificantly changes for the samples prepared under different conditions, but the intensity is usually about two times larger than that expected from the tochilinite composition and EDS data, probably, due to brucite nanoparticles attached to the tochilinite. The surface contamination can be eliminate through reducing the initial proportion of Mg/Fe reagents less to than 1, but the formation of iron hydr(oxide) by-products was observed for the atomic ratios Mg/Fe < 0.75. Another way is decreasing the excess of sodium sulfide (spectra *d* in Fig. 2), albeit this leads to enhanced content of Fe in hydroxide layers. Both the purity and composition of tochilinite can be modified via addition of cations entering the hydroxide layers; particularly, Al decreases both the amount of brucite impurity and the content of Fe in the hydroxide layers of tochilinite, while Li has an opposite effect (compare spectra a, b and c).

The X-ray photoelectron spectra of the valence band show the maximum at about 6 eV typical for O 3p states, and several unresolved step-like features at lower energies probably originating from Fe 3d orbitals hybridized, rather slightly, with S states. A strong peak near the VB edge characteristic of low-spin Fe^{2+} centers with the configuration $(e_g)^4$ $(t_g)^2$ (the notation of 3d orbitals suggests tetrahedral coordination of Fe) is absent. Similar features shifted to higher energies by 0.3-0.5 eV can be distinguished both in REELS spectra (Fig. S4) and UV-vis absorption spectra discussed below.

3.3. Mössbauer spectroscopy and magnetization study

^{57}Fe Mössbauer spectroscopy provides indispensable information on the oxidation and spin states of Fe atoms, chemical bonding and magnetic properties of iron-bearing materials. The room-temperature spectra of tochilinites acquired in the current research consist of asymmetric and wide doublets, as well as P(Δ) distributions, which can be fitted using several doublets with close hyperfine parameters (Fig. 3, Table 2). It is likely that, akin to valleriite [50], doublets with the chemical shift $\delta = 0.3$-0.4 mm/s and quadrupole splitting Δ of 0.4-0.6 mm/s are due to Fe^{3+}-S centers, and the ones with $\delta \geq 0.4$ mm/s and Δ of 1 ± 0.2 mm/s originate from high-spin Fe^{3+} cations in octahedral OH^- environment (Fe^{3+}-6OH), whereas the quantities of Fe^{2+}-OH centers ($\delta \sim 1$ mm/s, $\Delta > 2$ mm/s [40-42,56-60]) are minor. The electron densities and electric field gradients at Fe^{2+} nuclei in tetrahedral coordination to S are close to those for Fe^{3+}-6OH centers so their signals are difficult to resolve.

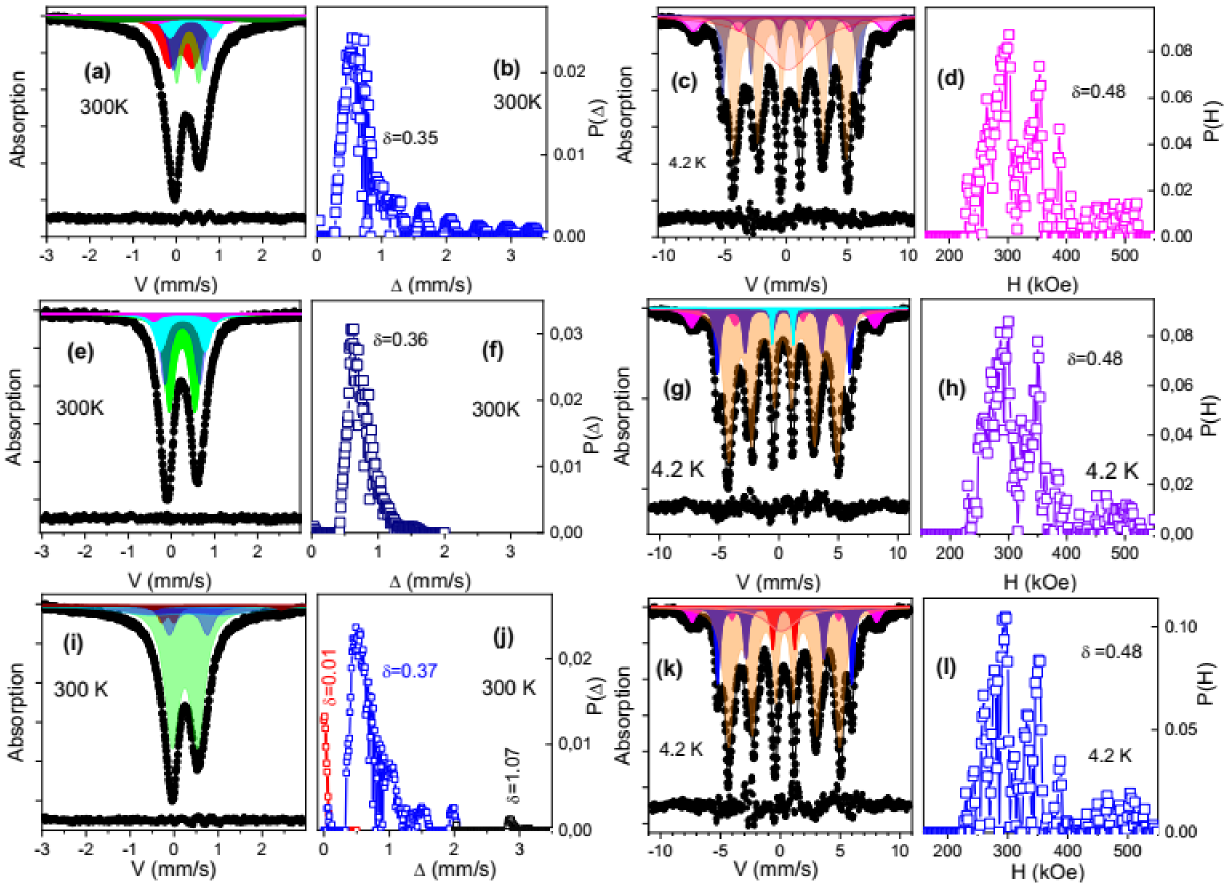

Fig. 3. Mössbauer spectra of tochilinites measured at room temperature (left panels) and 4.2 K from tochilinites synthesized with the initial proportions of precursors (a-d) Fe 2, Mg 1.5, S 15, (e-h) Fe 2, Mg 1.5, S 15, Al 0.5, (i-l) Fe 2, Mg 1.5, S 15, Li0.5. The points below the spectra are differences between the experimental results and fitted curves (colored lines).

The Mössbauer spectra measured at the temperature of 4.2 K consist of at least three six-line patterns together with a wide line from fast relaxation processes and a small doublet with the hyperfine parameters $\delta \approx 0.42$ mm/s and $\Delta \approx 1.8$ mm/s. The last features appear to be due to Fe^{3+} centers in strongly disordered paramagnetic hydroxide layers or (hydr)oxide nanoparticle admixture. The sextets with the hyperfine magnetic field H of ~480 kOe, 350 kOe and 290 kOe are signatures of magnetic ordering, with the field magnitude characterizing spin density on a site. Taking in mind that one unpaired electron corresponds to $H \sim 110$ kOe in oxide systems [69-71], so these values can be attributed to high-spin Fe centers with five, S=5/2, four (S = 2) and three unpaired electron (S=3/2), respectively. However, the interpretation is not straightforward because covalent bonding between Fe and S or OH ligands decreases the spin densities on the Fe nuclei. Valleriite containing Fe^{3+} in both the layers showed the H values from 330 kOe to 240 kOe [50], and the sextet with H approaching 500 kOe arose in the samples with the smaller content of Fe in hydroxide layers. We suggested that the lower hyperfine field corresponds to Fe^{3+}-6OH centers, as the higher H were ascribed to Fe^{3+} cations in the CuFeS$_2$-like sheets on the base of Fe distribution between the layers derived from XPS data. Therefore, it is most likely for tochilinite that the strongest six-line pattern with H = 288 mm/s, $\delta \sim 0.46$ mm/s, Δ = 0 mm/s is a superposition of the signals from Fe^{2+}-4S centers with the electronic 3d configuration of Fe^{2+} $(e_g\alpha)^2(e_g\beta)^1(t_g\alpha)^3$ (that is, S = 2), where α and β stay for major and minor electron spins, respectively, and from octahedral Fe^{3+}-6OH centers in the configuration $(t_{2g}\alpha)^3(e_g\alpha)^2$. The sextet with H =346 mm/s should be assigned to tetrahedral sites Fe^{3+}-4S with the high-spin 3d configuration $(e_g\alpha)^2(t_g\alpha)^3$, i.e. S = 5/2, in accord with the assignments of the room-temperature patterns. The low hyperfine field at the Fe^{3+} nuclei in hydroxide layers can be explained by the presence of OH$^-$ ligands and insignificant O^2 anions [67]. The largest field may be due to specific positions of high-spin Fe^{3+} cations in hydroxide layers in coordination with O^{2-} ligands.

Table 2. Parameters of fitting the Mössbauer spectra of tochilinites synthesized* (a) without doping and (b) doped with Al or (c) Li, measured at 298 K and 4.2 K. δ is a chemical shift relative to α-Fe (mm/s), Δ is a quadrupole splitting (mm/s), W - a width of a doublet line or internal 34 and external 16 lines for sextets (mm/s), H - internal magnetic field (kOe), A - a fraction of a particular iron position (%).

Sample	298 K					4.2 K					
	δ	Δ	W	A	Site	δ	H	Δ	W	A	Site
(a)	0.21	0.56	0.49	0.27	Fe^{2+}(4S)	0.60	490	-0.44	0.53-1.33	0.09	Fe^{3+}(6O)
	0.38	0.51	0.26	0.21	Fe^{3+}-4S	0.50	346	0.04	0.40-0.48	0.16	Fe^{3+}(4S)
	0.41	0.72	0.30	0.20	Fe^{2+}(4S) Fe^{3+}(6OH)	0.47	287	-0.02	0.44-0.79	0.47	Fe^{2+}(4S), Fe^{3+}(6OH)
	0.46	0.99	0.38	0.10	Fe^{3+}(6OH)	0.25	-	-	5.00	0.29	Relax
	0.45	1.60	0.77	0.07	Fe^{3+}(6OH,O)						
	0.46	3.21	2.04	0.15	Fe^{2+}(6OH)						
(b)	0.27	0.38	0.30	0.07	Fe^{3+}(4S)	0.70	480	-0.42	0.58-1.08	0.10	Fe^{3+}(6O)
	0.36	0.59	0.28	0.41	Fe^{3+}(4S)	0.51	346	0	0.46	0.15	Fe^{3+}(4S)
	0.37	0.81	0.28	0.30	Fe^{2+}(4S)	0.48	284	0	0.56-0.98	0.73	Fe^{2+}(4S), Fe^{3+}(6OH)
	0.38	1.03	0.32	0.18	Fe^{3+}(6OH)						
	0.41	1.41	0.31	0.03	Fe^{2+}(6OH,O)	0.44	-	1.76	0.21	0.02	Fe^{3+}(6OH,O)
(c)	-0.04	0.29	0.21	0.04	Fe^{2+}(4S)	0.49	480	-0.09	0.47-0.76	0.06	Fe^{3+}(6O)
	0.36	0.58	0.40	0.65	Fe^{3+}(4S)	0.50	349	-0.01	0.43	0.16	Fe^{3+}(4S)
	0.44	0.87	0.34	0.12	Fe^{2+}(4S), Fe^{3+}(6OH)	0.47	289	-0.02	0.52-0.98	0.65	Fe^{2+}(4S), Fe^{3+}(6OH)
	0.37	1.75	1.81	0.18	Fe^{3+}(6OH,O)	0.40	-	1.81	0.39	0.04	Fe^{3+}(6OH,O)
	1.09	2.90	0.28	0.01	Fe^{2+}(6O)	0.20	-	-	3.11	0.09	Relax

*Atomic proportions of reagents: (a) Fe 2, Mg 1.5, S 15, (b) Fe 2, Mg 1.5, S 15, Al 0.5, (c) Fe 2, Mg 1.5, S 15, Li 0.5

The spectra reported in the literature for tochilinites [35, 40-42] and mackinawite FeS [56-60] composed of similar tetrahedral sulfidic sheets connected with van-der-Waals forces typically show a narrow maximum from low-spin Fe^{2+}-S centers with δ ~ 0.4 mm/s at room temperature and about 0.47 mm/s at cryogenic temperatures, along with contributions of other Fe species formed as reaction by-products [40-42] or arose upon oxidation of the ferrous sulfide [57-60]. The hyperfine magnetic structure emerges in mackinawite since its aging causes deficit of Fe and S-S bonding, and also formation of high-spin Fe^{3+} and Fe^{2+} instead of singlet Fe^{2+}. Particularly, Schröder et al. [60] have assigned the six-line pattern with the hyperfine field of about 270 kOe to intermediate spin state Fe^{2+} sites (S=1) with distorted tetrahedral coordination to S, but our results for tochilinite infer rather high-spin Fe^{2+}-4S centers with S=3/2.

The SQUID magnetization study (Fig. 4) shows paramagnetic behavior of tochilinites at the temperatures down to 4.2 K. Some differences between FC and ZFC curves were observed for Al-doped tochilinite (b), i.e., with lower content of Fe in the hydroxide layers, demonstrating that the Fe-OH species promote spin disorder in the iron sulfide sheets. The findings imply an effect of Fe atoms located in hydroxide layers onto sulfide sheets, that is, a kind of 3D magnetic interactions between Fe atoms in these layers.

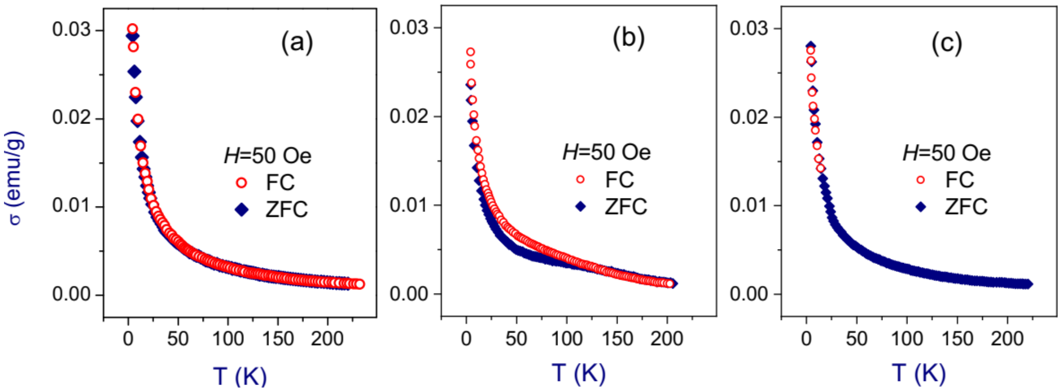

Fig. 4. Temperature dependences (FC and ZFC) of magnetization of tochilinites prepared using the atomic ratios of precursors (a) Fe 2, Mg 2, S 15, (b) Fe 2, Mg 2, S 15, Al 0.2, (c) Fe 2, Mg 2, S 15, Li 1.

In general, the Mössbauer spectroscopy and SQUID measurements confirm that the synthetic tochilinite contains both high-spin Fe^{3+} and Fe^{2+} centers in the sulfide layers while low-spin and intermediary spin Fe^{2+} are absent or negligible. The numbers of the Fe^{3+}/Fe^{2+} centers are comparable, in agreement with the results of XPS, but cannot be precisely determined owing to overlapping the Mössbauer signals from Fe^{2+}-4S and Fe^{3+}-6OH species both at 300 K and 4.2 K. This explains small changes of the spectra for different samples, although the spectrum of Al-doped samples with the smaller content of Fe-OH species is somewhat narrower at both temperatures.

3.3. Impedance spectroscopy

To determine transport characteristics of tochilinite nanoflakes, we measured *ac* impedance in the temperature range of 4.2 K to 300 K at frequencies from 40 Hz to 1 MHz; *dc* resistivity was high and poor reproducible because of an impeded electron transfer between the nanoflakes. Fig. 5 shows temperature dependences of imaginary part of dielectric permittivity ε`` recorded at a frequency of 1 kHz as example and dielectric loss tangent tan(δ) = ε``/ε` for particulate tochilinite samples; selected results for such tableted specimens are presented in Fig. S5 (Supporting information). The *ac* permittivity changes by about three orders of magnitude with the temperature and exhibits a characteristic response frequency at a peak temperature (T_p) for the frequency variation of the imaginary part ε``.

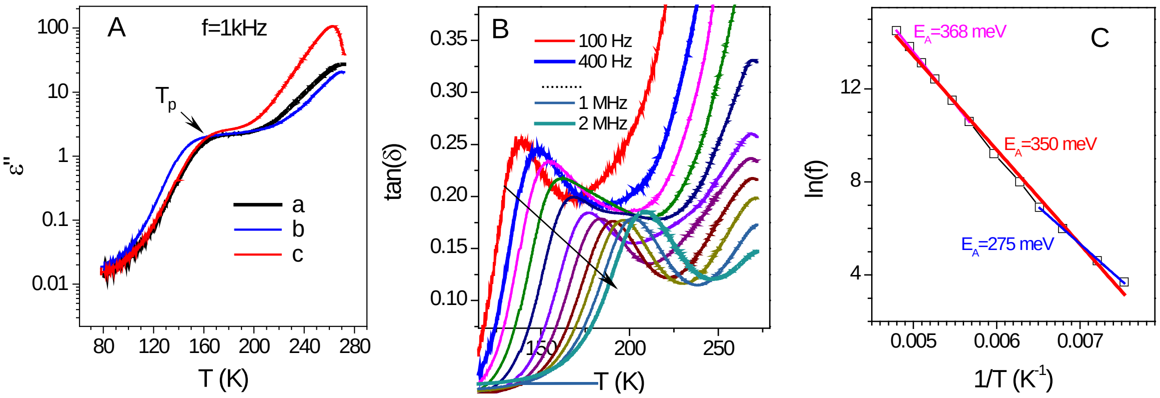

Fig. 5. A: Imaginary part of dielectric permittivity for tochilinites prepared with the atomic ratios of precursors (a) Fe 2, Mg 2, S 15, (b) Fe 2, Mg 2, S 15, Al 0.5, (c) Fe 2, Mg 2, S 15, Li 0.5. B: dielectric loss tangents at various frequencies as a function of temperature for the sample (b). (C): peak frequency vs reciprocal temperature (Arrhenius plot) for the sample (b).

As a first approximation, the temperature dependence of the characteristic frequency can be described by the Arrhenius relation [72-74]:

$$f = f_0 \exp(-E_a/k_B T) \ ,$$

where f is the characteristic frequency, $k_B T$ is the thermal energy, f_0 is a prefactor and E_a is the activation energy, which is 350-380 meV for all the samples, being slightly larger for the materials without dopants and lower for Al-doped tochilinite. Strictly speaking, the Arrhenius plots are not completely linear, and it can be described by activation energies up to 400 meV and down to 250 mV at high and low frequencies, respectively. If the materials are considered as a dielectric, the parameter f_0 is about $2{\cdot}10^{14}$ Hz for E_a = 360 meV and $\sim 2{\cdot}10^{11}$ Hz for E_a = 270 meV as determined by extrapolating the Arrhenius plots. The first frequency typical for electron polarization is faster than the characteristic time of Mössbauer spectroscopy. The lower frequencies may be due to atomic or dipole fluctuations, although, for example, Ikeda et al. [72] have assigned similar values of f_0 and E_a in ferroelectric $LuFe_2O_4$ to the exchange of electrons between Fe^{2+} and Fe^{3+} at the domain boundary. We suggest that the above processes involve a few Fe 3d states in the fundamental gap having slightly different energies but distinct relaxation times.

3.4. UV-vis-NIR absorption spectra and zeta-potentials of hydrosols

The optical spectra of aqueous tochilinite colloids (Fig. 6, A) have a series of maxima A at ~700 nm (1.73 eV) and longer wavelengths, B at 460 nm (2.65 eV), C at 340 nm (3.8 eV), D at 265 nm (4.69 eV) and one more peak at 205 nm (5.95 eV), although that may be an artefact. The maxima slightly blueshift for the Al-doped samples having the reduced content of Fe in magnesium hydroxide layers, and the peak D is all but absent in such samples. Similar sets of maxima are known for iron-sulfur clusters in proteins, which play critical roles in central biological processes [75-80], and UV-vis-NIR spectroscopy of corresponding aqueous solutions is widely used to identify clusters (the real systems are commonly composed of a mixture of several cluster types) and to examine their structure [77-80]. The spectral features reflect the ligand-to-metal charge transfer transitions, involving bonding, non-bonding and antibonding σ orbitals of sulfur anions and Fe 3d states [79,80] as illustrated in simplistic band diagram in Fig.

6, B, while maxima of A-type at longer wavelengths are insignificant. The clusters denoted [2Fe-2S] are composed of iron atoms in tetrahedral coordination to S, including two S atoms in peptide molecules, either paramagnetic with alignment of Fe^{+2} and Fe^{3+} cations (S=1/2) or antiferromagnetic with two Fe^{3+} cations (S=0). The clusters $[1Fe\text{-}0S]^{2+/3+}$ with Fe^{2+} (S = 2) or Fe^{3+} (S = 5/2) in tetrahedral environment of S [75-80] better agree with the Mössbauer spectroscopy findings (Fig. 3), suggesting insignificant alignment of neighboring electron spins in tochilinite. In this case, the peak C is believed to correspond to the reduced $[1Fe\text{-}0S]^{2+}$ clusters with Fe^{2+} cations, and the main maximum at 490 nm (peak D) is characteristic of $[1Fe\text{-}0S]^{3+}$ clusters exhibiting also several minor spectral features [79]. Exact nature and positions of the features are dependent of the type of Fe-S clusters and specific S-containing organic ligands (peptides or proteins) [75-80]. In turn, the spectra of tochilinite may be affected by the non-stoichiometry defects and S-S bonding in the $Fe_{1-x}S$ layer and Fe content in hydroxide ones, which need to be studied. Anyway, the interpretation of the spectra in terms of Fe-S clusters concurs with comparable numbers of sulfidic Fe^{2+} and Fe^{3+} centers.

The absorption at longer wavelengths nearby the maxima A is insignificant in the Fe-S clusters, so its nature in tochilinite is different. This is unlikely either the exciton absorption observed for semiconductor nanoparticles or localized surface plasmon resonance (LSPR) [81,82] because of low density of free electrons in the composites. The absorption may arise, akin to Fe-containing metal chalcogenides, including valleriite [50], from quasi-static dielectric resonance [83-85]. This effect are believed to take place in nanomaterials exhibiting a negative real permittivity at certain optical frequencies, in particular, for Fe 3d states forming a narrow intermediary band (IB) in the wide fundamental gap. The resonance redshifts for a narrower VB-IB gap [85] that is the case for tochilinite with the gap being about 0.3 eV (Fig. 6, B), in comparison with chalcopyrite and valleriite having the gap width of about 0.5 eV.

Otherwise, the phenomena can be described in terms of all-dielectric Mie resonance in insulating and semiconducting nanomaterials [86-88]. The absorption in the visible region is associated with the light scattering by subwavelength particles with low dielectric loses and high refractive index [86]. The above transport and impedance measurements suggest that tochilinite has the appropriate dielectric permittivity; particularly, ε' is approximately 11 at 2 MHz and low temperatures that is comparable with the value of ~12 for Si [87]. Moreover, the position of the major absorption maximum at ~700 nm, which is usually due to magnetic dipole resonance [86], is comparable to those for 160 nm silicon nanoparticles (the resonance size is on the order of $d \approx \lambda/n$, where n is its refractive index ($n \approx 4$ in Si), and λ is the light wavelength) [86,87]. This correlates well with the dimensions of the tochilinite flakes, and the shift of the maxima may be caused by slightly different size or properties of the particles. The peaks B, C, D may be associated with the electric dipole and magnetic and electric quadrupole resonances [86]. Such spectral patterns have been observed and attributed to the dielectric Mie resonances for WS_2 nanodisks [88] with the dimensions similar to those of tochilinite nanoflakes.

It is worth noting that the shoulders about 2.3, 3.3 and 4.4 eV below the VB edge (Fig. 2) are separated by ~1 eV as the C-D peaks in the UV-vis spectra and REELS but their binding energies are redshifted by ~0.3 eV that may be an energy gap between the VB edge and empty electron levels participating in the optical transitions and charge transport according the impedance measurements (Fig. 6, B). This hypothesis better correlates with the above assignment of the short-wavelength features to charge-transfer excitations rather than to the Mie resonances. If this is the case, the optical response of tochilinite probably combines the molecular-type Fe-S excitations and collective resonances, most likely, all-static dielectric Mie resonance [86-88].

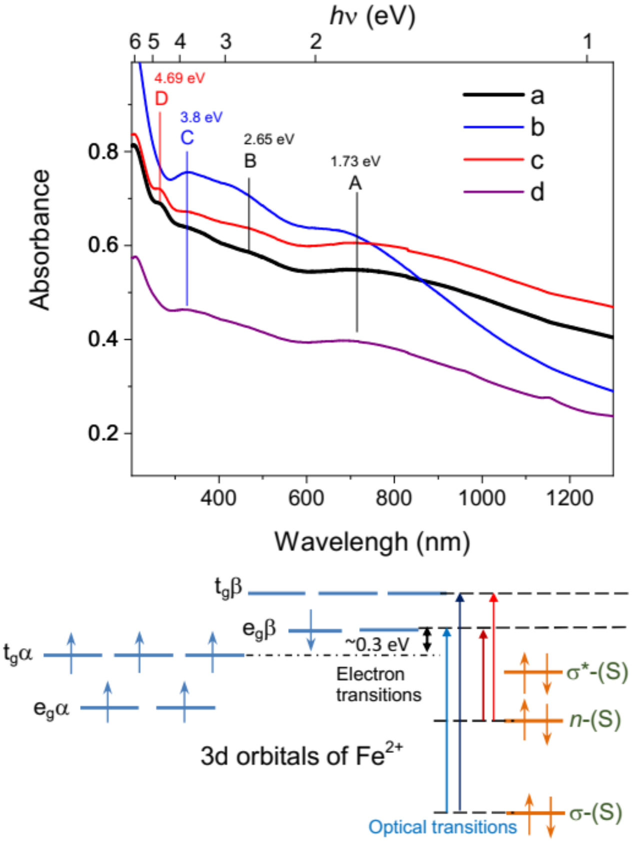

Fig. 6. UV-vis-NIR absorption spectra of aqueous colloids of tochilinite synthesized hydrothermally using the proportions of reagents (a) Fe 2, Mg 1.5, S 15, (b) Fe 2, Mg 1.5, S 15, Al 0.5, (c) Fe 2, Mg 1.5, S 15, Li 0.5, (d) Fe 2, Mg 1.5, S 15, Al 0.5, Li 0.5; and dispersed in water. Lower panel: Simplified diagram of the electron levels for Fe^{2+} cations assuming tetrahedral coordination (the levels for Fe^{3+} are omitted for clarity), S ligands, and optical transitions in the sulfide layer of tochilinite by analogy with Fe-S cluster in peptides [79,80].

3.6. Zeta-potential measurement and implications to the formation mechanism

Fig. 7, A shows average zeta potential vs pH plots measured for hydrosols of the synthetic tochilinites by changing pH from alkaline region to neutral media by adding 0.001 M HCl; we remind that pH of the reaction systems ranges from 10 to 12. Zeta potentials were essentially negative if excessive sodium sulfide was used in the synthesis, indicating a negative charge of the outer hydrophilic layers formed by brucite-type hydroxides, despite magnesium hydroxide and its derivatives typically have positive zeta potentials till very alkaline solutions [89] (see also curve *d* in Fig. 7, C). The effect of the precursor proportion Fe/Mg and Al or Li doping was insignificant. In contrast, the particles manufactured using the initial ratio Fe/S approached 1 exhibit negative potentials of low magnitudes, and even positive ones in neutral solutions. This appears to mean that the negative surface charge is largely due to sulfide anions adsorbed on the hydroxide sheets.

Zeta potentials of dispersions formed in early reaction stages before the hydrothermal treatment are presented in Fig. 7, B. The average zeta potential vs pH plots are similar to those in Fig. 7, A, and the frequency distributions of zeta potential were unimodal, implying that freshly precipitated sulfide and hydroxide components already reacted or, at least, aggregated as no separate particles of each sort exist in the dispersions. Zeta potentials of the individual precursors given in panel C confirm that Mg hydroxides, including in solutions containing Al (not presented in the Figure), are charged positively, and iron sulfide as well as iron hydroxide particles are negative, with the potential of those precipitated by excessive sodium sulfide is pH independent. The TEM examination (Fig. 7, D) revealed that the entities formed at room temperature are flakes thinner than 5 nm (the wire-like particles are the flakes exposed their edges) and rare nanotubes. The electron diffraction (Fig. 7, E) are close to brucite and pyrite, and EDS analysis (please, see EDS data and additional micrographs Fig. S6) found that, the concentration of Mg is higher than those of Fe and S, probably due to the sample handling and the decomposition under the electron beam with volatilization of sulfur. This seems to be the case for separate nanoparticles, which are discernible in some flakes. Nevertheless, the remaining nanosheets composed mainly of $Mg(OH)_2$ may be signature of their role in the formation of layered structure of tochilinites.

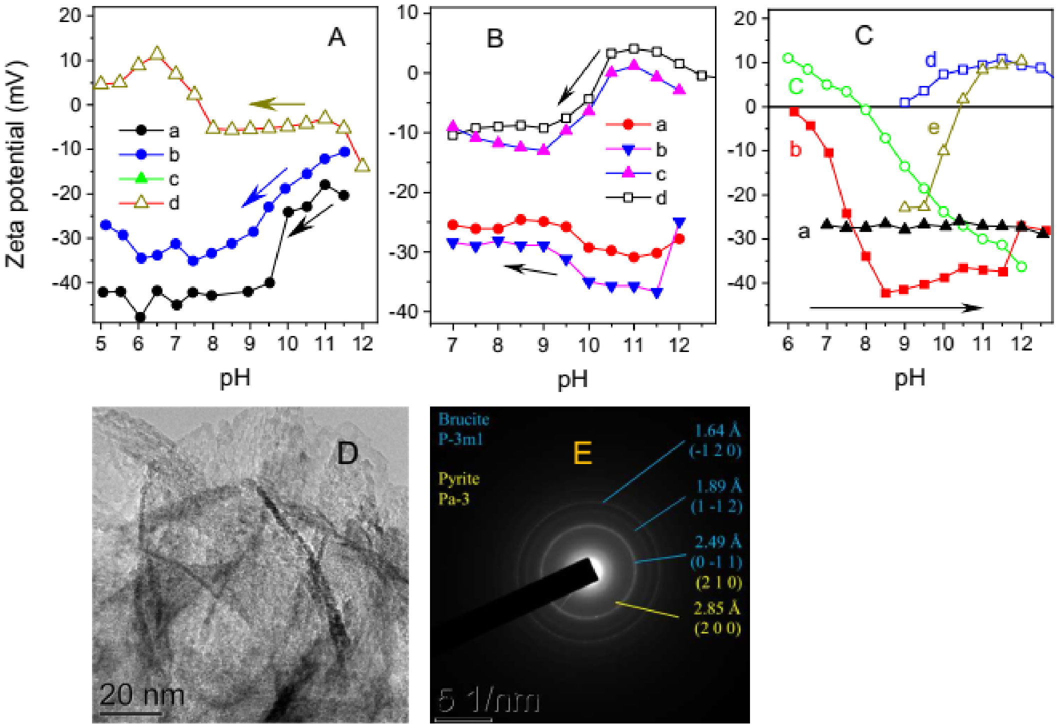

Fig. 7. pH dependences of zeta potentials and TEM data for the precursors and reaction products. Panel A: tochilinites after hydrothermal synthesis, washing and re-dispersion in water prepared with the reagent ratios (a) Fe 2, Mg 1.5, S 15, (b) Fe 2, Mg 1.5, Al 0.5, S 15, (c) Fe 2, Mg 1.5, S 2. Panel B: dispersions formed after room-temperature mixing the reagents at proportions (a) Fe 2, Mg 2, S 15, (b) Fe 2, Mg 1.3, S 15, (c) Fe 2, Mg 1.3, S 2, (d) Fe 2, Mg 2, S 2. Panel C: dispersions of precursor solutions at room temperature (a) Fe 1, S 7.5, (b) Fe 1, S 1, (c) iron hydroxide, (d) magnesium hydroxide, (e) magnesium hydroxide and sodium sulfide. Arrows indicate the directions of pH changes. (D) Typical TEM image and (E) SAED pattern are measured for the products formed at room temperature under the same conditions as the curve (a) in panel B.

4. Discussion

We have demonstrated herein that the two-dimensional sulfide-hydroxide material can be prepared with the high yield and negligible impurity phases in one-pot hydrothermal synthesis. The findings infer that the structure of tochilinite arises via layer-by-layer interaction of magnesium hydroxide and iron sulfide directed by their opposite electric charges, and the utilization of over-stoichiometric sulfide anions ensures the process robustness. Many mechanistic details still need to be clarified; in particular, the thickness growth of crystalline flakes that requires enhanced temperatures possibly involves a solid-state transfer of iron, sulfide anions and other species between and through the layers.

The previous synthetic studies [37-46] have been largely aimed at mimicking the mineral formation processes, including extra-terrestrial ones, and commonly used strict precautions against oxidation of the iron sulfide part of tochilinite, akin to mackinawite [57-60], to preserve low-spin Fe^{2+}. The materials manufactured here through the simple method contain high-spin ferric and ferrous cations, which are paramagnetic both at 293 and 4.2 K. At the same time, the low-temperature Mössbauer spectra show several magnetic ordered states attributed to the abovementioned iron centers in the sulfide layers, and Fe^{3+} coordinated to OH^- and minor O^{2-} ligands in Mg-based hydroxide sheets. The content of Fe in the hydroxide layers can be changed by doping the layers with Al or Li, but this only slightly affects the Mössbauer patterns and magnetization curves (Figs. 3 and 4). Nonetheless, the effect does exist (it is more noticeable in valleriite [50]) so the low-temperature magnetism can include an interlayer Fe-Fe interaction, i.e. 3D phenomena. We guess that the effect can be controlled by varying the concentration of O^{2-} anions, for example, via mild heating or drying. The possibility to tune the oxidation and spin state of iron with doping or even fully replacing iron with other 3d metals open additional prospects for their utilization in electronics and spintronics. Obviously, superconductivity and electron correlation phenomena are improbable in paramagnetic tochilinite. Tochilinite comprising of singlet ferrous iron has been obtained using both reducing media and the ratio of precursors Fe/S close to 1 [60]. This, however, complicates the procedure and makes it unstable, facilitating the formation of magnetite and other impurities, and decreasing the stability of tochilinite.

The paramagnetic material possesses numerous interesting properties, just few of which are mentioned in this article. Some of them are related to the layered two-dimensional structure; for example, specific thermal reactions of metal sulfide sheets confined between the hydroxide layers were found [27] (full data to be reported elsewhere). The non-trivial optical spectra of tochilinite reported, to the best of our knowledge, for the first time, were interpreted in terms of both all-dielectric Mie resonance and local S-Fe charge-transfer absorption. The resonant scattering in the visible and near-infrared regions depending on the particle dimensions pave the way for their engineering as nanoantennas and other applications in the emerging next-generation nanophotonics [86-88]. The optical maxima at shorter wavelengths are similar with those of ubiquitous iron – sulfur proteins and peptides, in which Fe-S clusters play the central role in cellular chemistry, including photosynthesis, cellular respiration, nitrogen fixation and other processes essential to life on earth biological catalysts [75-78]. These phenomena are due to a ladder of electron levels participating in charge transfer, and this hints that tochilinite-type materials can be active as catalysts, photocatalysts and electrocatalysts in a variety of reactions.

The current contribution highlights tochilinite-type composites as a member, along with valleriite, of the new platform of multifunctional 2D materials, which are cheap, eco-friendly and easily manufactured, and could be comparable with LDH, TMD, MXenes. Further studies on the materials properties are necessary to outline their potential.

5. Conclusions

The simple hydrothermal synthesis developed in this study yields tochilinite-type material $m(\mathrm{Fe}_{1-x}\mathrm{S})\cdot n(\mathrm{Mg,Fe})(\mathrm{OH})_2$ constructed by alternating quasi-atomic sheets of iron sulfide and magnesium-based hydroxide. The tochilinite was manufactured, with negligible content of by-products (mainly brucite $\mathrm{Mg(OH)_2}$), as flakes 100-200 nm in the lateral size and 10-20 nm thick. The materials were characterized using a set of methods including X-ray photoelectron and ^{57}Fe Mössbauer spectroscopies, magnetic and impedance measurements, zeta potentials and UV-vis-NIR spectroscopy for the aqueous colloids. It was established that the Fe-deficient sulfide sheets are composed of comparable amounts of high-spin Fe^{3+} and Fe^{2+} centers, and some S-S bonding in addition to monosulfide. The hydroxide layers contain Fe^{3+} rather than Fe^{2+} cations that amounts of 10-40% of total iron; the quantities of the Fe-OH species can be reduced by using Al and increased with Li modifiers with typical atomic precursor ratios Al/Fe (Li/Fe) from 0.1 to 0.5. The reliable synthesis is generally reached by utilizing large excess of sodium sulfide. Zeta potentials of the colloidal products were about -30 mV, while were close to zero for the Fe/S precursor ratio approached 1; the same picture was observed soon after mixing the reagents at room temperature. It was suggested that the self-assembly of the sulfide-hydroxide composite is driven by the opposite electric charges of iron sulfide and magnesium hydroxide sheets. The asymmetric doublets in room-temperature Mössbauer spectra were fitted with several doublets with the chemical shift 0.35-0.4 mm/s and gradually changing quadrupole splitting; three sextets at hyperfine fields of ~290, 350 and 480 kOe arose at 4.2 K were attributed to high-spin Fe^{2+}-4S centers overlapping signals Fe^{3+}-(6OH), Fe^{3+}-4S, and some Fe^{3+}-x(OH)y(O) centers in hydroxide layers, respectively. This indicates magnetic ordering at 4.2 K, with paramagnetic behavior found in SQUID experiments. Temperature and frequency dependences of the dielectric permittivity revealed the activation energy of about 0.3 eV, probably due to an electron transfer between Fe 3d states. Optical absorption at ~700 nm may be due to quasi-static dielectric resonance or, more likely, high-index all-dielectric Mie size-dependent resonance. Blue-shifted features in the spectra appear to arise from molecular–type ligand - Fe d charge transfer, like Fe-S clusters, probably, $[\mathrm{1Fe\text{-}0S}]^{2+/3+}$ type, in proteins. On the base of these results, some potential applications of tochilinites as a representative of the new family of multifunctional 2D materials, e.g., in the next-generation nanophotonics, (photo)- and (electro)catalysis, are briefly considered.

Supporting Information

Additional selected area electron diffraction patterns, elemental mapping, XPS and REELS data, dielectric permittivity data, TEM, EDS and SAED data on room-temperature reaction products.

Acknowledgements

This research was supported by the Russian Science Foundation, project 22-13-00321. Facilities of the Krasnoyarsk Regional Center of Research Equipment of Federal Research Center «Krasnoyarsk Science Center SB RAS» were employed in the work.

References

[1] M.-R. Gao, Y.-F. Xu, J. Jiang, S.-H. Yu, Nanostructured metal chalcogenides: synthesis, modification, and applications in energy conversion and storage devices, Chem. Soc. Rev. 42 (2013) 2986-3017. https://doi.org/10.1039/c2cs35310e.

[2] M. Xu, T. Lian, M. Shi, H. Chen, Graphene-like two-dimensional materials, Chem. Rev. 113 (2013) 3766–3798. https://doi.org/10.1021/cr300263a.

[3] A.A. Tedstone, D.J. Lewis, P. O'Brien, Synthesis, properties, and applications of transition metal-doped layered transition metal dichalcogenides, Chem. Mater. 28 (2016) 1965-1974. https://doi.org/10.1021/acs.chemmater.6b00430.

[4] D. Monga, S. Sharma, N.P. Shetti, S. Basu, K.R. Reddy, T.M. Aminabhavi, Advances in transition metal dichalcogenide-based two-dimensional nanomaterials, Mater. Today Chem. 19 (2021) 100399. https://doi.org/10.1016/j.mtchem.2020.100399.

[5] T. Gao, Q. Zhang, L. Li, X. Zhou, L. Li, H. Li, T. Zhai, 2D ternary chalcogenides, Adv. Optical Mater. 6 (2018) 1800058. https://doi.org/10.1002/adom.201800058.

[6] M.T. Edmonds, S.Y. Quek, U. Wurstbauer, S.M. Wu, N.R. Glavin, S. Das, S.P. Dash, J.M. Redwing, J.A. Robinson, and M. Terrones. Graphene and Beyond: Recent Advances in Two-Dimensional Materials Synthesis, Properties, and Devices. ACS Nanosci. Au (2022). https://doi.org/10.1021/acsnanoscienceau.2c00017.

[7] A.I. Khan and D. O’Hare. Intercalation chemistry of layered double hydroxides: recent developments and applications. J. Mater. Chem. 12 (2002) 3191–3198. https://doi.org/10.1039/b204076j.

[8] C.-H. Lin, H.-L. Chu, W.-S. Hwang, M.-C. Wang, and H.-H. Ko. Synthesis and optical properties of MgAl layered double hydroxides precursor powders. AIP Advances 7 (2017) 125005. https://doi.org/10.1063/1.4990832.

[9] G. Fan, F. Li, D.G. Evans, X. Duan. Catalytic applications of layered double hydroxides: Recent advances and perspectives. Chem. Soc. Rev. 43 (2014) 7040-7066. https://doi.org/10.1039/C4CS00160E.

[10] R. Tian, R. Liang, M. Wei, D.G. Evans, and X. Duan. Applications of Layered Double Hydroxide Materials: Recent Advances and Perspective. In: Mingos, D. (eds). 50 Years of Structure and Bonding – The Anniversary Volume. Structure and Bonding, vol. 172, 2016, pp. 65–84. Springer, Cham. DOI: 10.1007/430_2015_205.

[11] 2D Metal Carbides and Nitrides (MXenes). B. Anasori, Y. Gogotsi (eds). Springer Cham, 2019, 534 p. https://doi.org/10.1007/978-3-030-19026-2.

[12] Y.-W. Cheng, J.-H. Dai, Y.-M. Zhang, Y. Song, Two-dimensional, ordered, double transition metal carbides (MXenes): a new family of promising catalysts for the hydrogen evolution reaction, J. Phys. Chem. C 122 (2018) 28113-28122. https://doi.org/10.1021/acs.jpcc.8b08914.

[13] L. Verger, V. Natu, M. Carey, M.W. Barsoum, MXenes: an introduction of their synthesis, select properties, and applications, Trends Chem. 1 (2019) 656-669. https://doi.org/10.1016/j.trechm.2019.04.006.

[14] H. Kim, H. N. Alshareef, MXetronics: MXene-enabled electronic and photonic devices, ACS Materials Lett. 2 (2020) 55–70. https://doi.org/10.1021/acsmaterialslett.9b00419.

[15] A.K. Geim, I. V. Grigorieva, Van der Waals heterostructures, Nature 499 (2013) 419-425. https://doi.org/10.1038/nature12385.

[16] M. Xu, T. Lian, M. Shi, H. Chen, Graphene-like two-dimensional materials, Chem. Rev.113 (2013) 3766–3798. https://doi.org/10.1021/cr300263a.

[17] Z. Du, S. Yang, S. Li, J. Lou, S. Zhang, S. Wang, B. Li, Y. Gong, L. Song, X. Zou, P. M. Ajayan, Conversion of non-van der Waals solids to 2D transition-metal chalcogenides, Nature 577 (2020) 492-496. https://doi.org/10.1038/s41586-019-1904-x.

[18] S. Pei, Z. Wang, and J. Xia. Interlayer Coupling: An Additional Degree of Freedom in Two-Dimensional Materials. ACS Nano 16 (2022) 11498−11503. https://doi.org/10.1021/acsnano.1c11498.

[19] L.J. Cabri, A new copper-iron sulfide, Econ. Geol. 62 (1967) 910-925. https://doi.org/10.2113/gsecongeo.62.7.910.

[20] H.T. Evans Jr., R. Allman, The crystal structure and crystal chemistry of valleriite, Z. fur Kristallogr. 127 (1968) 73-93. https://doi.org/10.1524/zkri.1968.127.1-4.73.

[21] D.C. Harris, D.J. Vaughan, Two fibrous iron sulfides and valleriite from Cyprus with new data on valleriite, Am. Mineral. 57 (1972) 1037–1052.

[22] H. Nickel, D.R. Hudson, The replacement of chrome spinel by chromian valleriite in sulphide-bearing ultramafic rocks in Western Australia, Contrib. Mineral. Petrol. 55 (1976) 265-277. https://doi.org/10.1007/BF00371337.

[23] F.B. Waanders, H. Pollak, Mössbauer spectroscopy to characterize iron sulphides, South Afr. J. Sci. 95 (1999) 387-390.

[24] A. Mücke, Review on mackinawite and valleriite: Formulae, localities, associations and intergrowths of the minerals, mode of formation and optical features in reflected light, J. Earth Sci. Clim. Change 8 (2017) 1000419. https://doi.org/10.4172/2157-7617.1000419.

[25] Y.L. Mikhlin, A.S. Romanchenko, E.V. Tomashevich, M.N. Volochaev, Yu.V. Laptev, XPS and XANES study of layered mineral valleriite, J. Struct. Chem. 58 (2017) 1137–1143. https://doi.org/10.1134/S0022476617060105.

[26] Y.L. Mikhlin, M.N. Likhatski, O.A. Bayukov, Y.V. Knyazev, D.A. Velikanov, Y.V. Tomashevich, A.S. Romanchenko, S.A. Vorobyev, M.V. Volochaev, S.M. Zharkov, D.M. Meira, Valleriite, a natural two-dimensional composite: X ray absorption, photoelectron and Mössbauer spectroscopy and magnetic characterization, ACS Omega 6 (2021) 7533–7543. http://dx.doi.org/10.1021/acsomega.0c06052.

[27] Y. Mikhlin, M. Likhatski, A. Romanchenko, S. Vorobyev, Y. Tomashevich, O. Fetisova, O. Bayukov, Y. Knyazev, I. Nemtsev, S. Karasev, A. Karacharov and R. Borisov, Valleriite-containing ore from Kingash deposit (Siberia, Russia): Mössbauer and X-ray photoelectron spectroscopy characterization, thermal and interfacial properties, J. Sib. Fed. Univ. Chemistry 15 (2022) 303–317. http://dx.doi.org/ 10.17516/1998-2836-0294.

[28] I.V. Pekov, E.V. Sereda, V.O. Yapaskurt, Y.S. Polekhovsky, S.N. Britvin, N.V. Chukanov, Ferrovalleriite, $2(Fe,Cu)S\cdot1.5Fe(OH)_2$: validation as a mineral species and new data, Geol. Ore Deposits 55 (2013) 637-647. https://doi.org/10.1134/S1075701513080102.

[29] I.V. Pekov, V.O. Yapaskurt, Y.S. Polekhovsky, M.F. Vigasina, O.I. Siidra, Ekplexite $(Nb,Mo)S_2\cdot(Mg_{1-x}Alx)(OH)_{2+x}$, kaskasite $(Mo,Nb)S_2\cdot(Mg_{1-x}Al_x)(OH)_{2+x}$ and manganokaskasite $(Mo,Nb)S_2\cdot(Mn_{1-x}Al_x)(OH)_{2+x}$, three new valleriite-group mineral species from the Khibiny alkaline complex, Kola Peninsula, Russia, Mineral. Mag. 78 (2014) 663–679. https://doi.org/10.1180/minmag.2014.078.3.14.

[30] N.I. Organova, A.D. Genkin, V.A. Drits, S.P. Molotkov, O.V. Kuz'mina, A.L. Dmitrik, Tochilinite, a new sulfide-hydroxide of iron and magnesium. Zapiski Vsesoyuznogo Mineralogicheskogo Obshchestva, 100 (1971) 477-487 [in Russian].

[31] M. Fleischer, New mineral names, Am. Mineral. 57 (1972) 1552-1561.

[32] N.I. Organova, V.A. Drits, A.L. Dmitrik, Structural study of tochilinite. Part I. The isometric variety, Soviet Physics - Crystallography 17 (1973) 667-671; N.I. Organova, V.A. Drits, A.L. Dmitrik, Structural study of tochilinite. II. Acicular variety. Unusual diffraction patterns, Soviet Physics - Crystallography 18 (1974) 606-609.

[33] N. I. Organova, V.A. Drits, A.L. Dmitrik, Selected Area Electron Diffraction Study of a Type II “Valleriite-Like” Mineral, Am. Mineral. 59 (1974) 190–200.

[34] I.D.R. Mackinnon, M.E. Zolensky, Proposed structures for poorly characterized phases in C2M carbonaceous chondrite meteorites, Nature 309 (1984) 240; M.E. Zolensky, I.D.R. Mackinnon, Microstructures of cylindrical tochilinites, Am. Mineral. 71 (1986) 1201-1209.

[35] R.G. Burns and D.S. Fisher. Nanophase mixed-valence iron minerals in meteorites identified by cryogenic Mössbauer spectroscopy, Hyperfine Interactions 91 (1994) 571-576.

[36] L.G. Vacher, L. Truche, F. Faure, L. Tissandier, R. Mosser-Ruck, Deciphering the conditions of tochilinite and cronstedtite formation in CM chondrites from low temperature hydrothermal experiments, Meteoritics & Planet. Sci. 54 (2019) 1870–1889. https://doi:org/10.1111/maps.13317187.

[37] G.A. Kakos, T.W. Turney, T.B. Williams. Synthesis and structure of tochilinite: A layered metal hydroxide/sulfide composite. J. Solid State Chem. 108 (1994) 102-111. https://doi.org/10.1006/jssc.1994.1016.

[38] S.V. Kozerenko, N.J. Organova, V.V. Fadeev, L.O. Magazina, N.N. Kolpakova, L.A. Kopneva, Tochilinite produced in laboratory, Lunar and Planetary Science Conference, 27 (1996) 695-696.

[39] J.H.P. Watson, D.C. Ellwood, B.A. Cressey & R.A. Lidzey, The Adsorption of Heavy Metals by Tochilinite, an Iron Sulfide Material Produced by Chemical Precipitation: Analysis Using a Simple Theory of Chemisorption, Separation Sci. Technol. 40 (2005) 959-990. https://doi.org/10.1081/SS-200051963.

[40] N.I. Chistyakova, T.V. Gubaidulina, V.S. Rusakov, Mössbauer investigations of natural and synthetic tochilinite and valleriite, Czech. J. Phys. 56 (2006) E123–E131. https://doi.org/10.1007/s10582-006-0478-7.

[41] T.V. Gubaidulina, N.I. Chistyakova, V.S. Rusakov, Mössbauer study of layered iron hydroxysulfides: tochilinite and valleriite, Bull. Russ. Acad. Sci. Phys. 71 (2007) 1269–1272. https://doi.org/10.3103/S106287380709016X.

[42] N.I., Chistyakova, V.S., Rusakov, S.V., Kozerenko, V.V. Fadeev, Synthesis of Iron Sulfides: A Mössbauer Study. In: Mashlan, M., Miglierini, M., Schaaf, P. (eds) Material Research in Atomic Scale by Mössbauer Spectroscopy. NATO Science Series, vol 94. Springer, Dordrecht, 2003, pp 261–270. https://doi.org/10.1007/978-94-010-0151-9_27.

[43] M.E. Zolensky, I.D.R. Mackinnon, Microstructures of cylindrical tochilinites, Am. Mineral. 71 (1986) 1201-1209.

[44] Y. Peng, L. Xu, G. Xi, C. Zhong, J. Lu, Z. Meng, G. Li, S. Zhang, G. Zhang, Y. Qian, An experimental study on the hydrothermal preparation of tochilinite nanotubes and tochilinite–serpentine-intergrowth nanotubes from metal particles, *Geochim. Cosmochim. Acta* 71 (2007) 2858-2875. https://doi.org/10.1016/j.gca.2007.03.012.

[45] Y. Peng, G. Xi, C. Zhong, L. Wang, J. Lu, X. Sun, L. Zhu, Q. Han, L. Shi, M. Sun, Q. Li, M. Yu, M. Yin, An experimental study on the preparation of tochilinite-originated intercalation compounds comprised of $Fe_{1-x}S$ host layers and various kinds of guest layers, *Geochim. Cosmochim. Acta* 73 (2009) 4862-4878. https://doi.org/10.1016/j.gca.2009.05.061.

[46] Y. Peng, Y. Jing, Hydrothermal preparation of analogous matrix minerals of CM carbonaceous chondrites from metal alloy particles, Earth Planet. Sci. Lett. 408 (2014) 252-262. https://doi.org/10.1016/J.EPSL.2014.10.020.

[47] K. Iiishi, T. Tomisaka, T. Kato, S. Takeno, Syntheses of valleriite, Am. Mineral. 55 (1970) 2107-2110.

[48] A.E. Hughes, G.A. Kakos, T.W. Turney, T.B. Williams, Synthesis and structure of valleriite, a layered metal hydroxide/sulfide composite, J. Solid State Chem., 1993, 104, 422-436. https://doi.org/10.1006/jssc.1993.1178.

[49] S. Takeno, G.H. Moh, Syntheses of selenian valleriite, Mineral. Petrol. 50 (1994) 209-218. https://doi.org/10.1007/BF01164606.

[50] Y.L. Mikhlin, R.V. Borisov, S.A. Vorobyev, Y.V. Tomashevich, A.S. Romanchenko, M.N. Likhatski, A.A. Karacharov, O.A. Bayukov, Y.V. Knyazev, D.A. Velikanov, S.M. Zharkov, A.S. Krylov, S.N. Krylova, I.V. Nemtsev. Synthesis and characterization of nanoscale composite particles formed by 2D layers of Cu-Fe sulfide and Mg-based hydroxide. J. Mater. Chem. A. 10 (2022) 9621–9634. hpps://doi.org/10.1039/D2TA00877G.

[51] X.F. Lu, N.Z. Wang, H. Wu, Y.P. Wu, D. Zhao, X.Z. Zeng, X.G. Luo, T. Wu, W. Bao, G.H. Zhang, F.Q. Huang, Q.Z. Huang, X.H. Chen, Coexistence of superconductivity and antiferromagnetism in $(Li_{0.8}Fe_{0.2})OHFeSe$, Nature Mater. 14 (2015) 325–329. https://doi.org/10.1038/nmat4155.

[52] U. Pachmayr, F. Nitsche, H. Luetkens, S. Kamusella, F. Brückner, R. Sarkar, H.-H. Klauss, D. Johrendt, Coexistence of 3d-ferromagnetism and superconductivity in $[(Li_{1-x}Fe_x)OH](Fe_{1-y}Li_y)Se$, Angew. Chem. Int. Ed. 54 (2015) 293–297. https://doi.org/10.1002/anie.201407756.

[53] X. Dong, K. Jin, D. Yuan, H. Zhou, J. Yuan, Y. Huang, W. Hua, J. Sun, P. Zheng, W. Hu, Y. Mao, M. Ma, G. Zhang, F. Zhou, Z. Zhao, $(Li_{0.84}Fe_{0.16})OHFe_{0.98}Se$ superconductor: ion-exchange synthesis of large single-crystal and highly two-dimensional electron properties, Phys. Rev. B 92 (2015) 064515. https://doi.org/10.1103/PhysRevB.92.064515.

[54] X. Zhou, C. Eckberg, B. Wilfong, S.-C. Liou, H. K. Vivanco, J. Paglione, E. E. Rodriguez, Superconductivity and magnetism in iron sulfides intercalated by metal hydroxides, Chem. Sci. 8 (2017) 3781–3788. https://doi.org/10.1039/c6sc05268a.

[55] M. Guo, X. Lai, J. Deng, L. He, J. Hao, X. Tan, Y. Ren, and J. Jian. NaOH-Intercalated Iron Chalcogenides $(Na_{1-x}OH)Fe_{1-y}X$ (X = Se, S): Ion-Exchange Synthesis and Physical Properties. Inorg. Chem. 60 (2021) 8742−8753. https://doi.org/10.1021/acs.inorgchem.1c00713.

[56] D. Vaughan, M. Ridout, Mössbauer studies of some sulphide minerals. *J. Inorg. Nucl. Chem.* 33 (1971) 741–746. https://doi.org/10.1016/0022-1902(71)80472-4.

[57] L. Fournes, J-C. Grenier, C. Chanson, P. Bezdicka, A. Wattiaux & M. Pouchard, Use of in situ Mössbauer spectroscopy for electrochemical reactions involving ^{57}Fe. *Hyperfine Interact.* 57 (1990) 1829–1832. https://doi.org/10.1007/BF02405729.

[58] S. Boursiquot, M. Mullet, M. Abdelmoula, J.-M. Génin, J.-J. Ehrhardt, The dry oxidation of tetragonal FeS_{1-x} mackinawite. *Phys. Chem. Minerals*, 28 (2001) 600-611. https://doi.org/10.1007/s002690100193.

[59] M. Mullet, S. Boursiquot, M. Abdelmoula, J.-M. Génin, J.-J. Ehrhardt, Surface chemistry and structural properties of mackinawite prepared by reaction of sulfide ions with metallic iron. *Geochim. Cosmochim. Acta* 66 (2002) 829–836. https://doi.org/10.1016/S0016-7037(01)00805-5.

[60] C. Schröder, M. Wan, I.B. Butler, A. Tait, S. Peiffer and C.A. McCammon, Identification of Mackinawite and Constraints on Its Electronic Configuration Using Mössbauer Spectroscopy, Minerals 10 (2020) 1090. https://doi.org/10.3390/min10121090.

[61] A.P. Grosvenor, B.A. Kobe, M.C. Biesinger, N.S. McIntyre, Investigation of multiplet splitting of Fe 2p XPS spectra and bonding in iron compounds, Surf. Interface Anal. 36 (2004) 1564-1574. https://doi.org/10.1002/sia.1984.

[62] Yu.V. Knyazev, A.S. Tarasov, M.S. Platunov, A.L. Trigub, O.A. Bayukov, A.I. Boronin, L.A. Solovyov, E.V. Rabchevskii, N.N. Shishkina, A.G. Anshits. Structural and electron transport properties of $CaFe_2O_4$ synthesized in air and in helium atmosphere. J. Alloys Compnds 820 (2020) 153073. https://doi.org/10.1016/j.jallcom.2019.153073.

[63] D.A. Velikanov, High-sensitivity measurements of the magnetic properties of materials at cryogenic temperatures, Inorg. Mater. Appl. Res. 11 (2020) 801–808. https://doi.org/10.1134/S2075113320040413.

[64] Y. Mikhlin, A. Romanchenko, Y. Tomashevich, Surface and interface analysis of iron sulfides in aqueous media using X-ray photoelectron spectroscopy of fast-frozen dispersions, Appl. Surf. Sci. 549 (2021) 149261. https://doi.org/10.1016/j.apsusc.2021.149261.

[65] M. Fantauzzi, B. Elsener, D. Atzei, A. Rigoldi, A. Rossi, Exploiting XPS for the identification of sulfides and polysulfides, RSC Adv., 2015, 5, 75953–75963. https://doi.org/10.1039/C5RA14915K.

[66] Y. Mikhlin, Y Tomashevich, S. Vorobyev, S. Saikova, A. Romanchenko, R. Félix, Hard X-ray photoelectron and X-ray absorption spectroscopy characterization of oxidized surfaces of iron sulfides. Appl. Surf. Sci. 2016, 387, 796–804. https://doi.org/10.1016/j.apsusc.2016.06.190.

[67] Y. Mikhlin, V. Nasluzov, A. Romanchenko, Y. Tomashevich, A. Shor, R. Felix, Layered structure of the near-surface region of oxidized chalcopyrite ($CuFeS_2$): hard X-ray photoelectron spectroscopy, X-ray absorption spectroscopy and DFT+U studies, Phys. Chem. Chem. Phys. 19 (2017) 2749 – 2759. https://doi.org/10.1039/C6CP07598C.

[68] V. Nasluzov, A. Shor, A. Romanchenko, Y. Tomashevich, Y. Mikhlin, DFT + U and low-temperature XPS studies of Fe-depleted chalcopyrite ($CuFeS_2$) surfaces: a focus on polysulfide species, J. Phys. Chem. C 123 (2019) 21031–21041. https://doi.org/10.1021/acs.jpcc.9b06127.

[69] R.E. Vandenberghe, C.A. Barrero, G.M. da Costa, E. Van San and E. De Grave, Mössbauer characterization of iron oxides and (oxy)hydroxides: the present state of the art. Hyperfine Interact. 126 (2000) 247–259. https://doi.org/10.1023/A:1012603603203.

[70] B. Wareppam, E. Kuzmann, V.K. Garg & L.H. Singh, Mössbauer spectroscopic investigations on iron oxides and modified nanostructures: A review. J. Mater. Res. (2022). https://doi.org/10.1557/s43578-022-00665-4.

[71] Yu.V. Baldokhin, I.P. Suzdalev, V.E. Prusakov, D.A. Burnazyan, V.P. Korneev, L.V. Kovalenko, G.E. Folmanis, A Study of Nanostructures Formed in the Hydrogen Reduction of $Fe(OH)_3$. Russ. J. Phys. Chem. B 6 (2012) 81–88. https://doi.org/10.1134/S1990793112010034.

[72] N. Ikeda, H. Ohsumi, K. Ohwada, K. Ishii, T. Inami, K. Kakurai, Y. Murakami, K. Yoshii, S. Mori, Y. Horibe, H. Kitô, Ferroelectricity from iron valence ordering in the charge-frustrated system $LuFe_2O_4$, Nature 436 (2005) 1136–1138. https://doi.org/10.1038/nature04039.

[73] S. Yin, S. Yin, C. Guild, S.L. Suib, J. Menka, Magnetic properties of pure and Fe doped HoCrO3 thin films fabricated via a solution route, J. Magnet. Magnetic Mat. 428 (2016). https://doi.org/10.1016/j.jmmm.2016.12.021.

[74] K. Dey, A. Ghosh, P. Modak, A. Indra, S. Majumdar, S. Giri, Tuning of multiferroic orders correlated to oxygen stoichiometry in magnetite films, Appl. Phys. Lett. 105 (2014) 142905. https://doi.org/10.1063/1.4897629

[75] D.C. Johnson, D.R. Dean, A.D. Smith, M.K. Johnson, Structure, function, and formation of biological iron-sulfur clusters. Annu. Rev. Biochem. 74 (2005) 247−281. dx.doi.org/10.1146/annurev.biochem.74.082803.133518.

[76] R.H. Holm, W. Lo, Structural Conversions of Synthetic and Protein-Bound Iron−Sulfur Clusters, Chem. Rev. 116 (2016) 13685−13713. dx.doi.org/10.1021/acs.chemrev.6b00276.

[77] C. Bonfio, L. Valer, S. Scintilla, S. Shah, D.J. Evans, L. Jin, J.W. Szostak, D.D. Sasselov, J.D. Sutherland and S.S. Mansy. UV-light-driven prebiotic synthesis of iron–sulfur clusters. Nature Chem. 9 (2017) 1229-1234. dx.doi.org/10.1038/NCHEM.2817.

[78] I.O. Betinol, S. Nader, S.S. Mansy, Spectral decomposition of iron-sulfur clusters. Anal. Biochem. 629, 2021, 114269. dx.doi.org/10.1016/j.ab.2021.114269.

[79] L. Valer, D. Rossetto, S. Scintilla, Y.J. Hu, A. Tomar, S. Nader, I.O. Betinol, S.S. Mansy, Methods to identify and characterize iron–sulfur oligopeptides in water, Can. J. Chem. 100 (2022) 475–483 dx.doi.org/10.1139/cjc-2021-0237.

[80] A. Kubas, Characterization of charge transfer excited states in [2Fe–2S] iron–sulfur clusters using conventional configuration interaction techniques, Theor. Chem. Acc. 139 (2020) 120. https://doi.org/10.1007/s00214-020-02635-7.

[81] A. Agrawal, S.H. Cho, O. Zandi, S. Ghosh, R.W. Johns, D.J. Milliron, Localized surface plasmon resonance in semiconductor nanocrystals, Chem. Rev. 118 (2018) 3121−3207. https://doi.org/10.1021/acs.chemrev.7b00613.

[82] M.N. An, H. Song, K.S. Jeong, Intraband transition and localized surface plasmon resonance of metal chalcogenide nanocrystals and their dependence on crystal structure, CrystEngComm. 24 (2022) 3828-3840. https://doi.org/10.1039/D2CE00312K.

[83] S. Ghosh, T. Avellini, A. Petrelli, I. Kriegel, R. Gaspari, G. Almeida, G. Bertoni, A. Cavalli, F. Scotognella, T. Pellegrino, L. Manna, Colloidal $CuFeS_2$ nanocrystals: intermediate Fe d-band leads to high photothermal conversion efficiency, Chem. Mater. 28 (2016) 4848-4858. https://doi.org/10.1021/acs.chemmater.6b02192.

[84] R. Gaspari, G. Della Valle, S. Ghosh, I. Kriegel, F. Scotognella, A. Cavalli, L. Manna, Quasi-static resonances in the visible spectrum from all-dielectric intermediate band semiconductor nanocrystals, Nano Lett. 17 (2017) 7691−7695. https://doi.org10.1021/acs.nanolett.7b03787.

[85] S. Lee, S. Ghosh, C. E. Hoyer, H. Liu, X. Li, V.C. Holmberg, Iron-content-dependent, quasi-static dielectric resonances and oxidative transitions in bornite and chalcopyrite copper iron sulfide nanocrystals, Chem. Mater. 33 (2021) 1821–1831. https://doi.org/10.1021/acs.chemmater.0c04798.

[86] A.I. Kuznetsov, A.E. Miroshnichenko, M.L. Brongersma, Y.S. Kivshar, B. Lukanchuk. Optically resonant dielectric nanostructures. Science. 354 (2016) 6314. https://doi.org/10.1126/science.aag2472.

[87] U. Zywietz, A.B. Evlyukhin, C. Reinhardt, B.N. Chichkov. Laser printing of silicon nanoparticles with resonant optical electric and magnetic responses. Nature Commun. 5 (2014) 3402. https://doi.org/10.1038/ncomms4402.

[88] R. Verre, D.G. Baranov, B. Munkhbat, J. Cuadra, M. Käll, and T. Shegai, Transition metal dichalcogenide nanodisks as high-index dielectric Mie nanoresonators, Nature Nanotechnol. 14 (2019) 679–683. https://doi.org/10.1038/s41565-019-0442-x
[89] M. Kosmulski, Isoelectric points and points of zero charge of metal (hydr)oxides: 50 years after Parks' review, 238 (2016) 1–61. doi.org/10.1016/j.cis.2016.10.005; M. Kosmulski, The pH dependent surface charging and points of zero charge. IX. Update, Adv. Colloid Interf. Sci. 296, (2021) 102519. https://doi.org/10.1016/j.cis.2021.102519.